



Numerical Simulation with a DES Approach for a High-Speed Train Subjected to the Crosswind

J. Zhang^{1,2}, K. He^{1,2}, X. Xiong^{1,2}, J. Wang^{1,2} and G. Gao^{1,2†}

¹ Key Laboratory of Traffic Safety on Track of Ministry of Education, Changsha, Hunan 410075, China

² School of Traffic & Transportation Engineering, Central South University, Changsha, Hunan 410075, China

†Corresponding Author Email: gjgao@csu.edu.cn

(Received January 2, 2017; accepted April 20, 2017)

ABSTRACT

A Detached Eddy Simulation (DES) method based on the SST $k-\omega$ turbulence model was used to investigate the instantaneous and time-averaged flow characteristics around the train with a slender body and high Reynolds number subjected to strong crosswinds. The evolution trends of multi-scale coherent vortex structures in the leeward side were studied. These pressure oscillation characteristics of monitoring points on the train surfaces were discussed. Time-averaged pressure and aerodynamic loads on each part of the train were analyzed in here. Also, the overturning moment coefficients were compared with the experimental data. The results show that the flow fields around the train present significant unsteady characteristics. Lots of vortex structures with different intensities, spatial geometrical scales, accompanied by a time change, appear in the leeward side of the train, in the wake of the tail car and below the bottom of the train. The oscillation characteristics of the flow field around the train directly affect the pressure change on the train surfaces, thereby affecting the aerodynamic loads of the train. The loads of each car fluctuate around some certain mean values, while the positive peak values can be higher than the mean ones by up to 34%. The load contributions of different parts to the total of the train are also obtained. According to it, to improve the crosswind stability of the high-speed train, much more attention should be paid on the aerodynamic shape design of the streamlined head and cross section. In addition, this work shows that the DES approach can give a better prediction of vortex structures in the wake compared with the RANS solution.

Keywords: High-speed train; Load contribution ratio; Vortex structure; DES; Crosswind.

NOMENCLATURE

C_s	side force coefficient	Re	Reynolds number
C_l	lift force coefficient	S	reference area
C_M	overturning moment coefficient	t	calculation time
C_p	static pressure coefficient	U	upstream velocity
C_t	non-dimensional time	v_w	wind velocity
h	train height	v_t	train speed
k	turbulent kinetic energy		
L	total length of the train	ε	dissipation rate
Q	second invariant of the velocity gradient tensor	ω	specific dissipation rate
W	train width	ρ	air density

1. INTRODUCTION

The flow around high-speed trains is characterized by highly turbulent and three-dimensional separations, especially under strong crosswinds. When the trains are running through these wind environments, the flow structure around them and the surface pressure distributions would be changed

significantly. Consequently, larger fluctuant aerodynamic loads would have great effects on the operational safety and lower the running stability with an increasing risk of overturning. In the past, to understand the flow around the trains and to improve their crosswind stability, many scholars and research institutes, at home or abroad, have done a series of investigations according to the full-

scale tests (Fujii *et al.* 1999, Matschke *et al.* 2000, Baker *et al.* 2004, Li 2011, Central South University 2011), wind tunnel tests (Fujii *et al.* 1999, Baker *et al.* 2004, Orellano and Schober 2006, Tanemoto *et al.* 2006, Cheli *et al.* 2010a and 2010b) and numerical simulations (Khier *et al.* 2000, Hemida and Krajnovic 2010, Mao *et al.* 2011, Ma *et al.* 2008, Yang *et al.* 2008, Zhang *et al.* 2011, Miao and Gao 2012, Nakade 2014), obtaining a lot of achievements, such as aerodynamic forces acting on the train, flow characteristics around the train and some preventive measures (shape optimization and regulation operation of the train, windbreak wall).

From the aspect of numerical simulation, Khier *et al.* (2000) used the three-dimensional, steady RANS equations and $k-\varepsilon$ turbulence model to simulate the airflow structures around a simplified high-speed train, studied the effect of yaw angles on the flow field. They discovered that flow separation takes place on both the lower and upper leeward edges, and the vortex structure clearly depends on the yaw angle. However, no separation from the windward edges was observed. Hemida and Krajnovic (2010) investigated the influence of two nose lengths (long nose and short nose) and two yaw angles (90° and 35°) on the time-averaged and instantaneous flows around a generic train model using Large-eddy simulation method. They found that the LES is a suitable to predict the flow structures around the train, and at different yaw angles the vortex structures are significantly different. In the case of the 90° the flow is dominated by unsteady vortex shedding with high frequency. In contrast, at 35° yaw angle, the attached and detached wake vortices dominate over the unsteady vortex shedding. In addition, the short nose would lead to highly unsteady and three-dimensional flow around the nose yielding more vortex structures in the wake. As a consequence it arises the dominating frequencies due to the shear layer instabilities. Mao *et al.* (2011) simulated the flow structures around the train and the aerodynamic forces on the train at the speed of 300 km/h using a uniform and an atmospheric boundary layer velocity profiles based on the SST $k-\omega$ turbulence model. Obviously, in the simulations, using the former one to assess the operation safety of the train subjected to a crosswind is a little over - conservative, which may decrease the limited train speed under strong winds. Ma *et al.* (2008) and Yang *et al.* (2008) studied the unsteady flow characteristics of a 2-D and a 3-D train models based on LES, and analyzed the unsteady aerodynamic force characteristics, which showed that the dominant frequency of the vortices is actually close to the natural frequency of some train structures. Zhang *et al.* (2011) simulated the aerodynamic performance of trains with 3 kinds of cross sections at different wind speeds, train speeds and yaw angles, and thought lower train height and larger round radius between the top and sides would be better to the crosswind stability of the train. Miao and Gao (2012) conducted the research on the crosswind stability of a simplified high-speed train at 5 different yaw angles using Detached Eddy Simulation. Nakade (2014) performed the

simulation on a very simple train model using Large Eddy Simulation in a turbulent boundary layer. The pressure coefficient distributions on the train surface were obtained from numerical simulations and wind tunnel tests, and the running effects on the aerodynamic characteristics of trains were discussed between the running and stationary conditions. Besides, some researchers also focus on the effect of the infrastructure scenario on the aerodynamic performance of trains under strong crosswinds, such as Diedrich *et al.* (2008) on the embankment, Liu and Zhang (2013) and Zhang *et al.* (2015) on the cutting, Zhang *et al.* (2013) on the bridge, and so on.

However, due to the computer resources available at that time, these studies above always use Reynolds-Averaged Navier–Stokes (RANS) approaches to solve the flow structures of a train with bogies, inter-carriage gaps or pantographs, or adopt Detached Eddy Simulation and Large Eddy Simulation methods to obtain the instantaneous characteristics around the train with a very simple and generic geometry. Although the results come from the RANS turbulence models show that they are very successful in predicting many parts of the flow around a train, they are weak to predict instantaneous characteristics in the leeward and wake regions. In fact, the Large-eddy Simulation (LES) method is good at capturing the instantaneous characteristics around the train (Hemida and Krajnovic 2010, Nakade 2014, Osth and Krajnovic 2014). However, it takes up massive computer demands. Therefore, there is a growing need for the attention to find a powerful numerical method to solve the flow characteristics around a reduced real shape train model with complex bogies and inter-carriage gaps. Meantime, according to the paper written by Hemida and Krajnovic (2010), at the a certain yaw angle there are a series of shedding vortices in the leeward and wake regions, which would enhance the oscillating magnitude to the objects along the railway, pose a risk to the surrounding environment and lower the crosswind stability of the train.

The objective of this study is to evaluate the capabilities of Detached Eddy Simulation (DES) for the simulation of high-speed train flow in a crosswind at a 20° yaw angle when the upstream velocity $U=60$ m/s. This yaw angle also corresponds to the train speed of 300 km/h and crosswind speed of 30 m/s. According to the "Interim measures for the management of Beijing–Tianjin intercity railway" (TG-QT106-2008), when the wind speed reaches above 30 m/s, the high-speed train is not allowed to run into the gale region. However, in our work, we want to improve the train speed running across the strong wind regions to a large extent, so choosing the 20° yaw angle to investigate the cross effect on a high-speed train is very important.

As to DES, this kind of method has been already used to investigate the flow around the train in open air without crosswinds (Flynn *et al.* 2014, Huang *et al.* 2016, Zhang *et al.* 2016). The instantaneous flow structures, oscillated pressure at monitoring

points, time-averaged static pressure distributions and aerodynamic forces are discussed in the following sections.

This paper is organized as follows. In Section 2, the numerical method and the Detached Eddy Simulation used in the present paper are described. In Section 3, the geometry of the train with complex bogies and inter-carriage gaps, the computational domain, and the boundary conditions are presented. The accuracy of the numerical method is discussed in Section 4. After that, in Section 5 the instantaneous flow structures, the time-averaged flow structures, the pressure coefficient and the aerodynamic forces are reported. Finally, conclusions are drawn in Section 6.

2. NUMERICAL METHOD

As a new research tool, the DES method has been widely used to predict the aerodynamic forces and high-Reynolds number separated flows around ground transport vehicles (Favre *et al.* 2011, Guilmineau *et al.* 2011, Miao and Gao 2012, Flynn *et al.* 2014). This model, which was first proposed by Spalart and Allmaras (1997), is a hybrid Reynolds-averaged Navier-Stokes–Large-Eddy Simulation (RANS–LES) method. It was developed to overcome the excessive computer demands of LES while seeking to improve on the accuracy of RANS in unsteady flows. In the DES approach, the unsteady RANS models are employed in the near-wall regions, while the filtered versions of the same models are used in the regions away from the near-wall (Fluent Inc 2011). For this hybrid method, a smooth transition is made from the regions where the unsteady Reynolds-averaged equations are solved to those where a standard LES is performed. The switching between the two models depends on the local grid-resolution (Fluent Inc 2011).

In the present study, the DES with SST $k-\omega$ model was utilized (Fluent Inc 2011). The SST $k-\omega$ model was developed by Menter (1994) to effectively blend the robust and accurate formulation of the $k-\omega$ model in the near-wall region with the free-stream independence of the $k-\varepsilon$ model in the far field. To achieve this, the $k-\varepsilon$ model is converted into a $k-\omega$ formulation. The SST $k-\omega$ model is similar to the standard $k-\omega$ model, but includes the following refinements (Fluent Inc 2011):

- The standard $k-\omega$ model and the transformed $k-\varepsilon$ model are both multiplied by a blending function and both models are added together. The blending function is designed to be one in the near-wall region, which activates the standard $k-\omega$ model, and zero away from the surface, which activates the transformed $k-\varepsilon$ model.
- The SST model incorporates a damped cross-diffusion derivative term in the ω equation.
- The definition of the turbulent viscosity is modified to account for the transport of the turbulent shear stress.
- The modeling constants are different.

These features make the SST $k-\omega$ model more accurate and reliable for a wider class of flows (for example, adverse pressure gradient flows, airfoils, transonic shock waves) than the standard $k-\omega$ model.

3. GEOMETRY AND COMPUTATIONAL PARAMETERS

The high-speed train model used for the numerical simulations is the same as the one in the wind tunnel tests (Zhang *et al.* 2013) is shown in Fig. 1. It consists of 3 three cars that are the head, middle and tail coaches with complex bogies and inter-carriage gaps, but without the pantograph and accessory structures. The length of the head car is 25.45 m at full scale not including the length of the inter-carriage gaps, while the middle coach is 24.50 m. The total length of the train is denoted by L . The train height h is 3.70 m and its width W is 3.38 m. The area of the cross section is 11.22 m². In the simulation, the model scale is 1/15th, which was constructed by referring to the model used in the wind tunnel tests, seeing the paper written by Zhang *et al.* (2013). The reference axis (X,Y,Z) is linked to the model. The origin of these axes is located on the horizontal plane of rail level and in the symmetry planes of the model. In this simulation, the Reynolds number, based on the train height, is $Re=1.0\times 10^6$.

The computational domain is shown in Fig. 2 starts at $20h$ in front of the train model and extends to $40h$ behind the model. The width of the domain is $30h$ with the model located at $10h$ far from the crosswind inlet, and the height is $10h$, which gives a blockage ratio of about 1.5%. After that, the flow near the train would not be affected by the boundary conditions.

For the boundary conditions used in this simulation, no slip walls are used for the train body geometry. The floor of the computational domain is set as a moving wall to realize the relative motion between the train and the ground. The roof is treated as symmetry. According to the paper written by Mao *et al.* (2011), using a uniform velocity profile could be much safer for a train running across the strong wind regions, so at the inlets, a uniform upstream velocity U that is a resultant velocity of the train speed along the X axis and crosswind speed along the Y axis is imposed, while at the outlet the pressure of 0 is imposed.

A free, open source CFD mesh generator package - SnappyHexMesh in OpenFOAM (Open Field Operation and Manipulation) - was utilized to build the mesh around the train (Openfoam, 2014). This tool offers an automatic grid generation method, which allows for grid refinement in the wall-normal direction around the research objective and generates the hexahedral and polyhedral mesh efficiently and quickly. Before a decision on the mesh resolution used is made, two cases with different numbers of cells have been tried: coarse and fine meshes consisting of 18 million and 26 million cells, respectively. In addition, compared

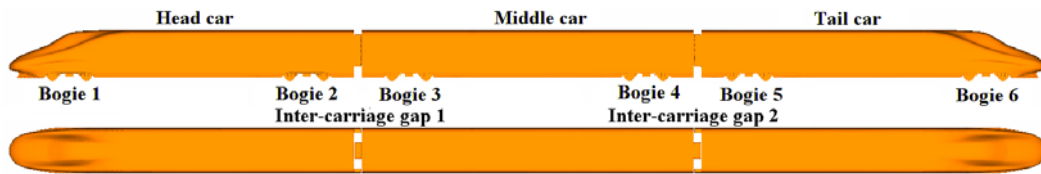


Fig. 1. Train model.

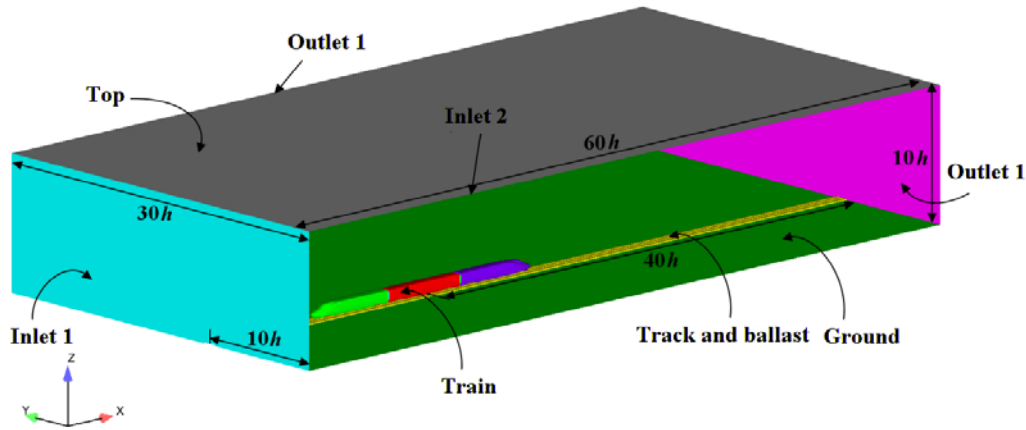


Fig. 2. Computational domain.

with the data from wind tunnel tests in Section 4, the coarse mesh and the numerical method are suitable for computing the flow field around the train subjected to a crosswind. The grid distributions are presented in Fig. 3. Due to the fast change of flow structure around the train surface and in the wake, a refinement box is built. In addition, to capture the flow near the wall correctly, a prism layer of 10 cells is created in a belt around the train. The thickness of the first layer is 0.32 mm at the 1/15th-scale model to ensure the use of wall functions in the turbulence model.

In this simulation, the Finite Volume Method (FVM) based on cell centers was adopted for the discretization of the controlling equations. Simulations were performed using a pressure-based solver. The SIMPLEC (Semi-Implicit Method for Pressure-Linked Equations Consistent) algorithm was used in the computational method to couple the pressure and the velocity field. A bounded central differencing scheme was chosen for solving the momentum equation. A second-order upwind scheme was chosen to solve the k and ω equations. The time derivative was discretized using the second-order implicit scheme for unsteady flow calculation. The convergence criterion is based on the residual value of continuity equation being less than 10^{-4} with minimal fluctuation. Convergence was also monitored by plotting the aerodynamic force coefficients on the train with time steps.

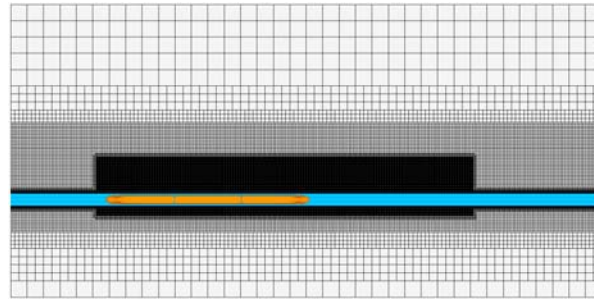
In all cases, the time step used is 0.0001s. It takes 1777 time steps corresponding to $C_t=48$ for one flow through passage, and the non-dimensional time is defined as " $C_t = tU / S^{1/2}$ ". After 2 passages, the flow is considered to be fully developed, seeing Fig. 4, and start to average the flow field. The

averaging time is about 0.5 s or 5000 time steps.

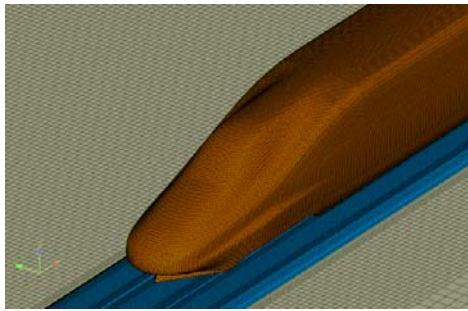
4. ACCURACY OF THE NUMERICAL METHOD

The experiments were conducted in the test section of the wind tunnel in the Low Speed Aerodynamic Institute of China Aerodynamics Research & Development Center (CARDC). The cross-sectional area of the tunnel in the test section is $8 \times 6 \text{ m}^2$, and to decrease the thickness of boundary layers a fixed ground board mounted on a turntable was installed. A 1/15th-scale train model consisted of three cars was placed on a flat ground board with the incoming flow speed set at 60 m/s. The model is with respect to the upstream velocity by a yaw angle of 20° corresponding to $v_t = 300 \text{ km/h}$ and crosswind speed $v_w = 30 \text{ m/s}$. The literatures (Sterling *et al.* 2008, Hemida H, Krajnovic 2010, Tian 2007) points out that when the Reynolds number is 3×10^5 in the numerical calculations, the flow around the train is in the turbulent state. With the increase of the Reynolds number, aerodynamic coefficients are not expected to change significantly.

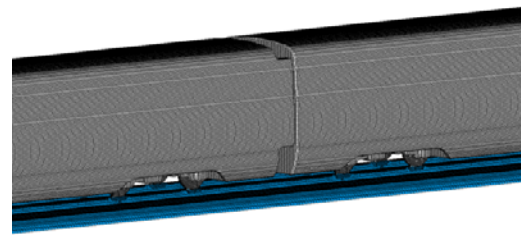
Table 1 shows the overturning moment coefficients C_M for all cases. These results are compared with the experimental data of Zhang *et al.* (2013). In this paper, the reference area is $S=0.0556 \text{ m}^2$, the characteristic height is h and the air density is $\rho = 1.225 \text{ kg/m}^3$. The other relevant definition of the side force coefficient C_s , lift force coefficient C_l and static pressure coefficient C_p can also be found in literatures (Baker *et al.* 2004, Orellano and Schober 2006, Diedrichs *et al.* 2008, Hemida and Krajnovic, 2010, Zhang *et al.* 2011, Wang *et al.* 2014).



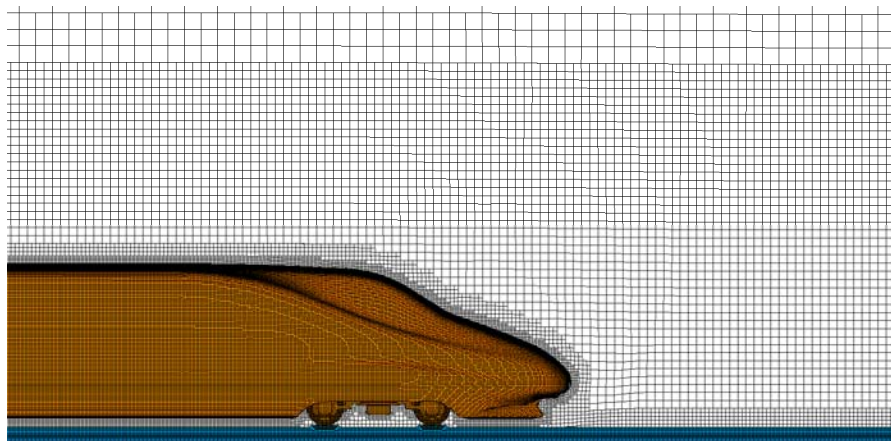
(a) Global mesh and refine box



(b) Mesh distribution around the head car



(c) Mesh distribution around the train body



(d) Mesh distribution on the tail car and in the wake

Fig. 3. Computational mesh.

To realize the relative motion between the train and the ground, a moving floor was used in this paper. However, in wind tunnel tests, the train model was fixed on a stationary floor, so there is a contradiction between expectation and reality. It is a very expensive methodology to simulate cases using DES with the stationary floor that is the same as the one used in the wind tunnel tests and just to validate the numerical method. To save computing resources, first a comparison was made between the simulation using a steady SST $k-\omega$ turbulence model with the stationary floor and wind tunnel tests, which shows reasonable agreement, particularly for the middle car. Then the boundary conditions of ground in both steady and unsteady cases were changed to investigate how the turbulence models affect the aerodynamic forces. And we found some differences on the forces, which is the expectation.

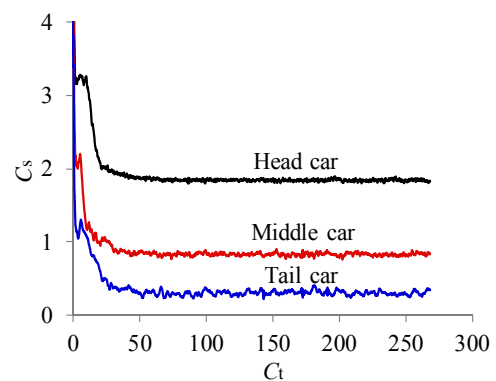


Fig. 4. Time history curves of C_s for each car.

According to Table 1, the errors for the head car are a little large, but less than 10%, while for the train set they are below 5%. The numerical results

Table 1 Overturning moment coefficients

Case	Ground condition	Head coach	Middle coach	Tail coach	Train set
Steady SST $k-\omega$	Stationary wall	-1.199	-0.688	-0.372	-2.259
	Moving wall	-1.236	-0.709	-0.359	-2.304
DES (SST $k-\omega$)	Moving wall	-1.234	-0.686	-0.386	-2.306
Wind tunnel test	Stationary wall	-1.14	-0.70	-0.38	-2.22
Error 1		5.18%	-1.71%	-2.11%	1.76%
Error 2		8.42%	1.29%	-5.53%	3.78%
Error 3		8.24%	-2.00%	1.58%	4.87%

Note: Error 1 is the error of data between the simulation with the Steady SST $k-\omega$ turbulence model in a stationary ground condition and experiment. Error 2 is the error of data between the simulation with the Steady SST $k-\omega$ turbulence model in a moving ground condition and experiment. Error 3 is the error of data between the simulation with the DES (SST $k-\omega$) turbulence model in a moving ground condition and experiment.

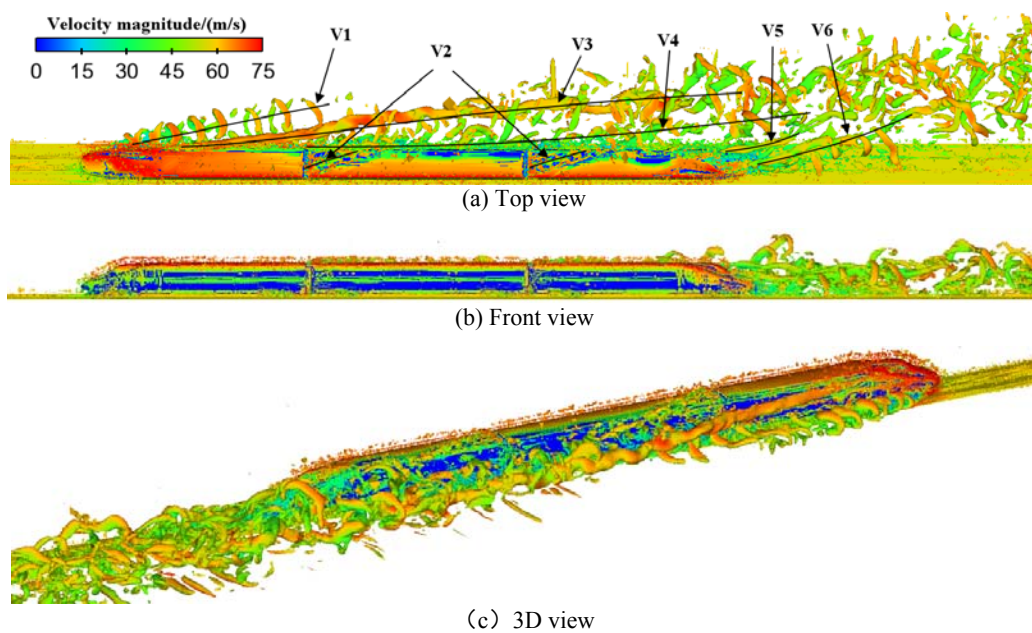


Fig. 5. Iso-surface of $Q=50000$ over the train and in the wake region.

obtained with stationary ground are very close to these experimental data. However, after using moving ground to simulate the relative motion between the train and the ground, these errors seems to be larger. For the results obtained with the Steady SST $k-\omega$ and DES (SST $k-\omega$) turbulence models in the moving ground condition, there is a bigger difference on the load of the tail car, which shows the DES method is better to capture the instantaneous flow characteristics in the wake. In general, the results obtained by numerical simulations using the Steady SST $k-\omega$ and DES (SST $k-\omega$) methods can be used to study the aerodynamic performance of the train under crosswinds.

5. RESULTS AND DISCUSSION

5.1 Vortex Structures

The vortex structures are always used to analyze the

instantaneous flow field. To identify the vortex regions, the Q criterion (Hunt *et al.* 1988), the second invariant of the velocity gradient tensor, is defined. Fig. 5 shows an iso-surface of Q ($Q=50000$) for the DES approach, which is colored with the velocity magnitude. The vortices are clearly visible in the leeward side and the wake of the train, forming the vortex structures V1 ~ V6. These similar flow patterns can also be found in the work of Copley (1987), Khier *et al.* (2000), Hemida and Krajnovic (2010) and Yao *et al.* (2014). Vortices V1, V3 and V4 generate and evolve from the streamlined head of the head car (Copley 1987, Khier *et al.* 2000, Hemida and Krajnovic 2010, Yao *et al.* 2014). Vortex V1 develops towards the rear in a spiral way, and gradually moves away from the train body. After travelling a distance of nearly a train length, it disappears. However, vortices V3 and V4 develop along the train length direction until they emerge into the wake region. Due to the

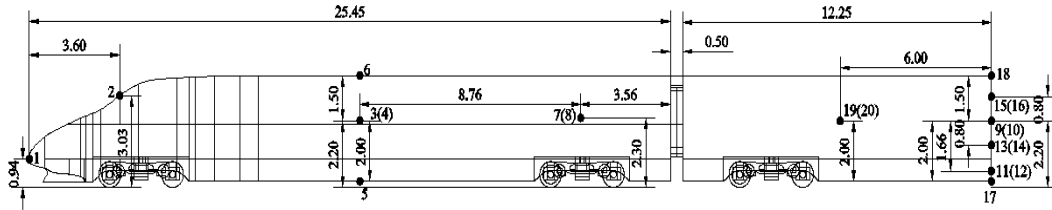


Fig. 6. Monitoring points on the train surface.

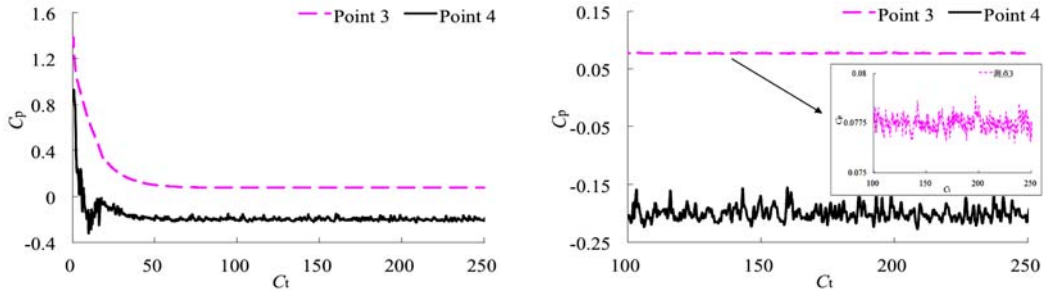


Fig. 7. Time history curves of C_p . Right figure is close-up.

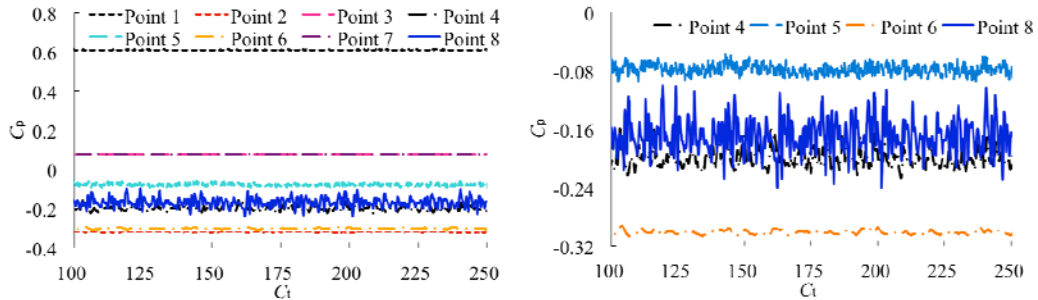


Fig. 8. Time history curves of C_p at monitoring points on the head car (Right figure is close up for some special points).

effect of the airflow from the top of the train, vortex V3 is located outside the vortex V4. The inter-carriage gaps destroy the continuous interface between the streamlined head coach and middle coach, which results in the flow separation, consequently a vortex V2 comes into being. This kind of vortex is not discovered in the previous work for all of train models are without inter-carriage gaps. However, due to its weak vortex strength, the vortex V2 is swallowed by vortices V3 and V4. Vortices V5 and V6 generate from the streamlined head of the tail car (Yao *et al.* 2014). Because the vortex intensity of the vortices V4 and V6 is stronger than the vortex V5, under the interaction effect of the both vortices, the vortex V5 disappears quickly. In the wake region, vortices V3, V4 and V6 gradually merge, and become weak.

5.2 Instantaneous Pressure of Monitoring Points on the Train Surface

To analyze the instantaneous pressure characteristics on the train surface, several monitoring points is symmetrical about the middle car are set up, as shown in Fig. 6, including 8 points on the head car, 14 points on the middle car and 8 points on the tail car. The monitoring points in the

round brackets presents they are on the leeward side of the train.

The time history curves of C_p at points 3 and 4 are demonstrated in Fig. 7, while right figure is close-up. The non-dimensional time C_t from 0 to 100 is not considered in calculating the averaged quantities, since these time-steps correspond to a transient period when the flow becomes unsteady. However, as time increases the solution values become relatively steady. These quantities are then calculated by taking the average value over the non-dimensional time from 100 to 250. The pressure oscillation at the measuring point 4 on the leeward side is more obvious than that at the measuring point 3, and this phenomenon can also be obtained by the analysis of the flow field structure (see Fig. 5).

The time history curves of C_p at monitoring points on the train surface are shown in Figs. 8~10. These pressure coefficients clearly fluctuate around some certain mean values, separately. On the windward side of the train body, C_p is positive or negative with small oscillation, such as at points 1, 3, 7, 9, 19, 23 and 27. However, the oscillation magnitudes

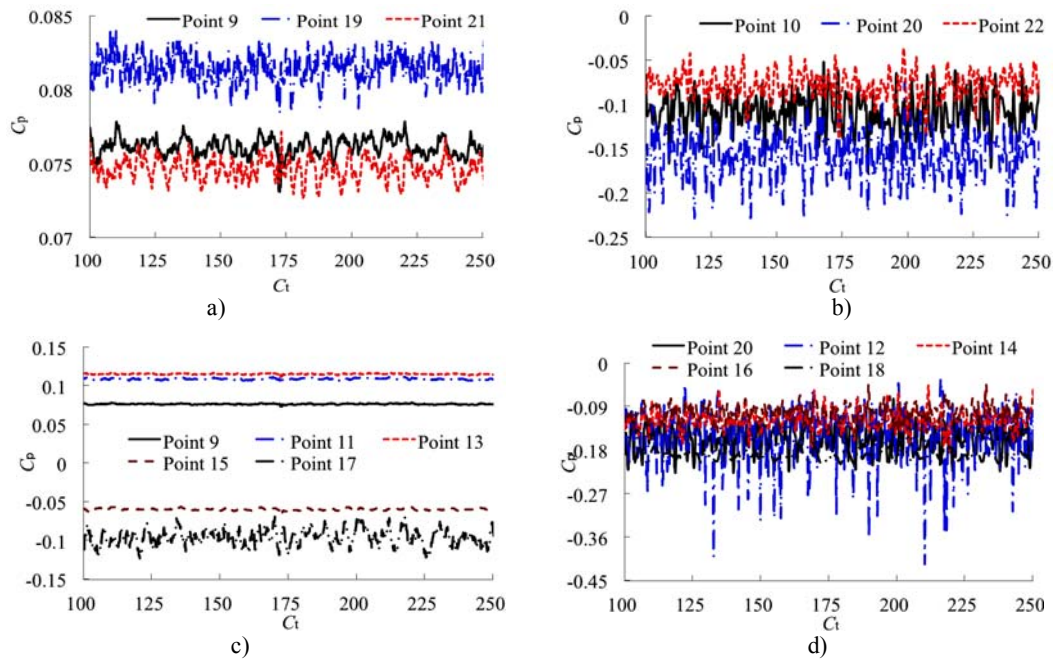


Fig. 9. Time history curves of C_p at monitoring points on the middle car: (a) Points at the same height on the windward side, (b) Points at the same height on the leeward side, (c) Points at the same cross section on the leeward side, (d) Points at the same cross section on the leeward side.

of C_p at the points on the leeward side, on the bottom and on the top of the train are a little larger, especially at these points such as points 4, 8, 10, 20, 24 and 28 on the leeward side and point 30 in the wake. In addition, when the point is close to the ballast and ground on the leeward side of the train, its oscillation would be stronger, seeing point 12. All of these shows the complex vortices have significant effects on the pressure variation on the train body (see Fig. 5). As a result, the time history curves of aerodynamic loads by the integral method will present some oscillation around mean values, separately.

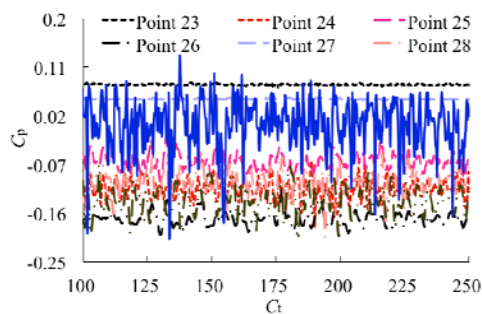


Fig. 10. Time history curves of C_p at monitoring points on the tail car.

Table 2 shows the pressure oscillation magnitudes and time-averaged values of several points on the train surface except of the windward side, for there is no separation on the windward side to cause pressure oscillation. Due to vortex development and separation, overall, the pressure fluctuations of

points on the leeward side are larger, while these on the bottom and the top are relatively less. And the pressure fluctuations of points on the head car are a little weaker than these on the middle and tail cars.

5.3 Time-Averaged Pressure on the Train Surface

Figure 11 shows the time-averaged static pressure coefficient on the train surface. In order to highlight the surface pressure distributions on different parts, the pressure coefficient range is set at $-0.69 \sim 0.23$.

The pressure on the streamlined head is affected by the complicated curved surface, which presents diversified distributions, while the pressure on the body with a uniform cross section shows more regular.

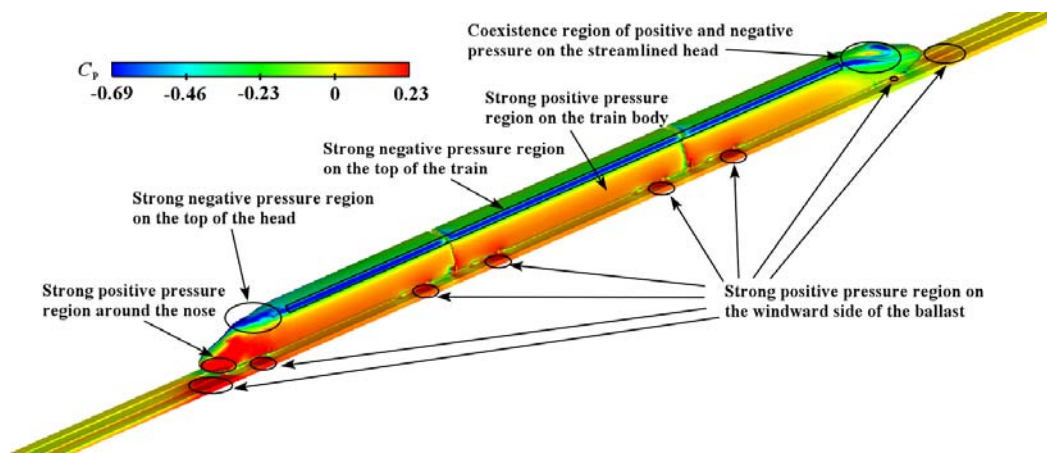
On the windward side of the train, the head car, middle car and most parts of the tail car are suffered positive pressure. However, on the streamlined head of the tail car, as the change of the cross-sectional shape causes vortex shedding from the head surface, there is a strong negative pressure area. Therefore, even on the windward side there are still some negative pressure regions. In addition, due to the blockage of the operator cab, a small positive pressure generates on the windward side.

In the leeward region around the train, as a result of the crosswind, the vortices separate from the train body and move downstream, as shown in Fig. 5. The head car, middle car and most parts of the car are suffered negative pressure. However, on the streamlined head of the tail car, local positive pressure is presented around the nose.

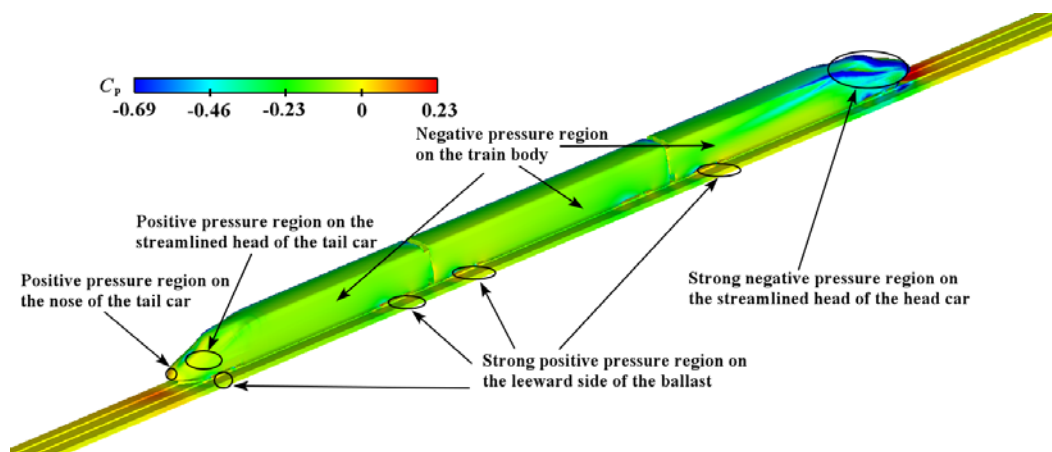
The maximum of positive pressure appears on the

Table 2 Oscillation statistics of C_p at monitoring points

Car	Point	Oscillation range	Oscillation magnitude	Time-averaged value
Head car	4	-0.15~-0.23	0.08	-0.200
	8	-0.10~-0.24	0.14	-0.169
	5	-0.05~-0.10	0.05	-0.078
	6	-0.29~-0.31	0.02	-0.301
Middle car	10	-0.05~-0.18	0.13	-0.109
	20	-0.07~-0.23	0.16	-0.157
	22	-0.03~-0.14	0.11	-0.079
	17	-0.06~-0.13	0.07	-0.096
	18	-0.16~-0.22	0.06	-0.192
Tail car	28	-0.04~-0.21	0.17	-0.102
	24	-0.06~-0.19	0.13	-0.116
	25	-0.02~-0.11	0.09	-0.065
	26	-0.11~-0.20	0.09	-0.170



(a) On the windward side



(a) On the leeward side

Fig. 11. Time-averaged pressure distributions on the train.

windward side of the streamlined head (see Fig. 11(a)). On the leeward side and the top of the head, due to the flow separation, the flow velocity is accelerated, and then there is a strong negative

pressure region. The peak value of negative pressure turns up on the leeward side of the head. At the transition arc from the windward

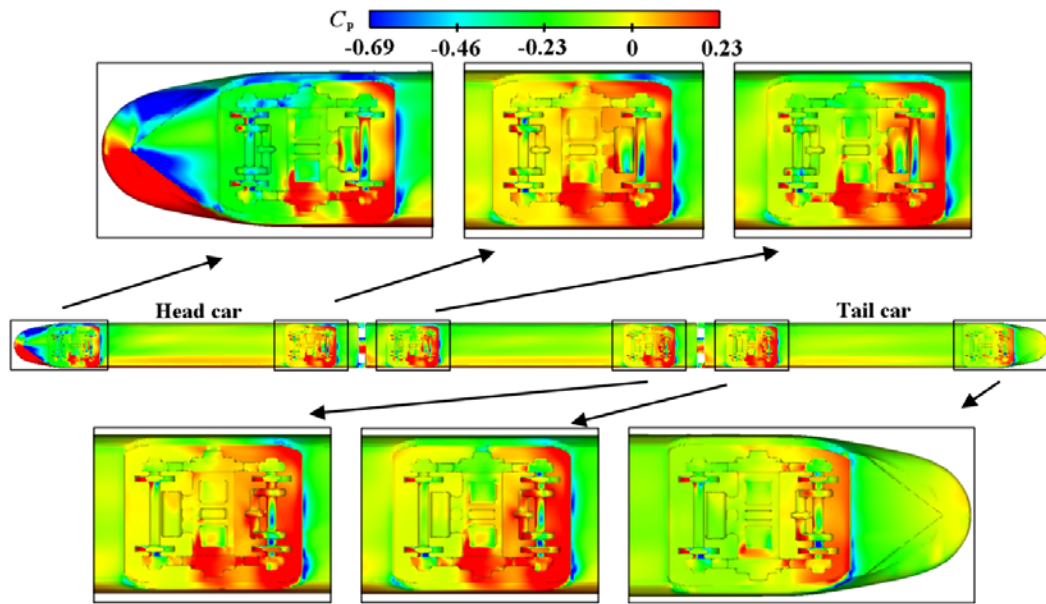


Fig. 12. Time-averaged pressure distributions on the bottom of the train.

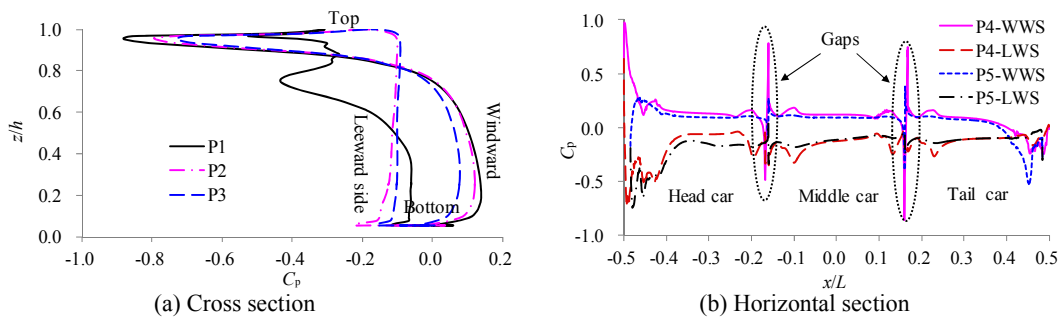


Fig. 13. Time-averaged pressure distributions on the cross section and horizontal section.

side to the top, where the flow is accelerated, strong negative pressure characteristics are presented inhere. The existence of the train changes the pressure distributions on the track bed accordingly. On these regions below noses and bogies, the pressure seems to be higher.

Figure 12 shows the time-averaged pressure distributions on the bottom of the train, including on the bogies. At the bottom of the train, a portion of area close to the windward side is shown as a positive pressure region (excluding the head area of the head and tail cars). In each bogie region, the front face of the equipment cabin is essentially a small positive or negative pressure. Blocked by the rear face of the equipment cabin, the strong positive area is concentrated in the latter half of the bogie region. In addition, except of the bogie 6 region (see Fig. 1), the other five bogie regions show strong positive pressure characteristics at the middle and the rear of the windward side.

In the bogie 1 area, due to the effect of the streamlined head and the flow impact on the front windward side of the head car, the flow beneath the train is accelerated so much that positive and

negative pressure regions on the comparison are very obvious. The bogie 2 and bogie 4 areas are almost in a positive pressure zone and the pressure distributions are very similar. The pressure at the rear end of the bogie 3 area is basically the same as that of the bogie 2, however, on the front end there is a small negative pressure zone. The front pressure distribution of the bogie 5 area is a little higher than that of the bogie 3, but lower than that of the bogie 4. On the rear part of the bogie 6 area the positive pressure is small, and on the front it is also basically in a small negative pressure.

To quantify the train surface pressure distributions, choose the cross section P1($x=-0.34L$), P2($x=0L$) and P3($x=0.34L$), and the horizontal section P4($z=0.25h$) and P5($z=0.53h$) for analysis, as shown in Fig. 13.

According to the mean pressure distributions on the curves of cross sections, on the windward side of the train is suffered positive pressure. Then a sharp decrease in pressure occurs at the transition arc from the upwind to the top, where the negative pressure extremes on the body section are also presented. Along the curves the pressure gradually

Table 3 Oscillation statistics of $C_{i(s,l,M)}$

$C_{i(s,l,M)}$	Car	Time-averaged value	Maximum positive peak	Error
C_s	Head car	1.840	1.891	2.8%
	Middle car	0.827	0.899	8.7%
	Tail car	0.302	0.405	34.0%
C_l	Head car	1.832	1.901	3.8%
	Middle car	1.289	1.377	6.8%
	Tail car	1.155	1.263	9.3%
C_M	Head car	1.234	1.260	2.1%
	Middle car	0.686	0.721	5.1%
	Tail car	0.386	0.434	12.4%

return to small negative pressure on the top. There is small positive pressure on the bottom of the train where is close to the windward side of the body. On the contrary, the bottom where is close to the leeward side is suffered small negative pressure. The C_p distribution on P1 is complicated, especially on the leeward side of the train, which indicates that the vortex on the leeward side directly influences the train surface pressure distribution. For all cross sections, the largest positive pressure turns up on the windward side of P1, while the lowest negative pressure generates on the transition arc of P1.

From the pressure distributions on the curves of the horizontal section, on the windward side of the train there is mainly positive pressure. The pressure of each car body gradually increases along the length of the train, but on the inter-carriage gaps, streamlined head of the train pressure changes sharply due to the small gap between two cars and the complex geometry of the head. In fact, the existence of the gap contributes to measuring the aerodynamic loads of each car in the wind tunnel tests, so in this simulation, a gap is also kept. However, for the train in operation, there is no this gap to cause such fast pressure change. In the wake, vortex separation from the tail head results in rapid reduction of pressure to negative values, but small positive pressure turns up on the small region around the nose. On the leeward side of the train, there is basically negative pressure, however, on P4 there is a certain region with positive pressure where is close to the nose. The pressure curves on the head fluctuate significantly, while the negative pressure on the body is more stable.

5.4 Aerodynamic Load Coefficients

Figure 14 shows the time history curves of aerodynamic load coefficients for each car. The loads present significant instantaneous characteristics that fluctuate around some certain mean values, while these peak values are much higher than the mean ones, as illustrated in Table 3. From the data we can see that the head car by the aerodynamic load the largest, followed by the middle car, the tail car's smallest aerodynamic load. For the fluctuation, C_s of the head car is relatively small as that of the tail car is largest; C_l of each car

is basically large with more obvious fluctuation for the tail car; the curves of C_M are affected by the combination with the side force and lift force, but they are mostly followed by the fluctuation trends of C_s .

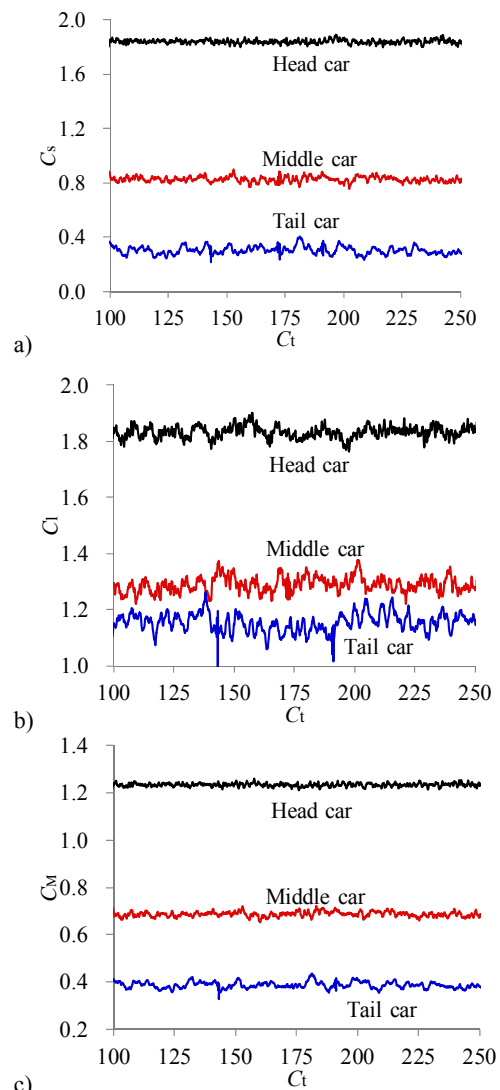


Fig. 14. Time history curves of aerodynamic load coefficients for each car: (a) C_s , (b) C_l , (c) C_M .

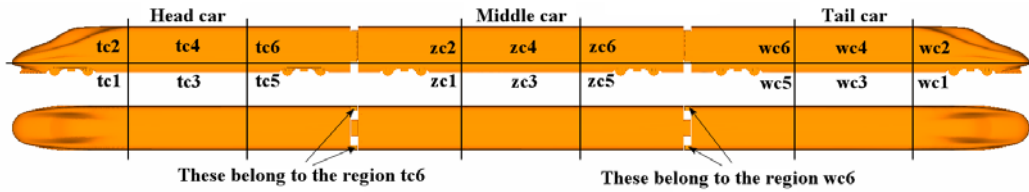


Fig. 15. Method of division for a high-speed train.

Table 4 Aerodynamic side coefficient C_s

Car	1	2	3	4	5	6	Train set
Head car	0.340	0.832	0.091	0.293	0.106	0.178	1.840
Middle car	0.178	0.230	0.118	0.121	0.109	0.071	0.827
Tail car	0.025	-0.220	0.083	0.066	0.145	0.203	0.302

Table 5 Aerodynamic lift coefficient C_l

Car	1	2	3	4	5	6	Train set
Head car	-0.220	0.754	-0.085	0.839	-0.121	0.665	1.832
Middle car	-0.146	0.618	-0.160	0.538	-0.117	0.556	1.289
Tail car	-0.151	0.467	-0.138	0.503	-0.113	0.587	1.155

Table 6 Aerodynamic overturning moment coefficient C_M

Car	1	2	3	4	5	6	Train set
Head car	-0.090	-0.519	-0.028	-0.345	-0.015	-0.237	-1.234
Middle car	-0.044	-0.259	-0.030	-0.178	-0.018	-0.157	-0.686
Tail car	0.020	0.026	-0.016	-0.141	-0.036	-0.239	-0.386

To explore the load contributions of different parts to the total of the train, each car is divided into 6 parts, as shown in Fig. 15. The time-averaged aerodynamic load coefficients of high-speed trains obtained from the simulation case are given in Table 4 for the aerodynamic side coefficient C_s , Table 5 for the aerodynamic lift coefficient C_l and Table 6 for the aerodynamic overturning moment coefficient C_M .

In the case of side forces, the region 2 of the tail car is suffered a negative force, which means the force is in an opposite direction to the crosswind. Except of this region, others are positive. Of the side force the head car, make up 62% in the total aerodynamic side force of the train (3-car grouping model); the middle car constitutes about 28%; the tail car only accounts for 10%. For the head car, the side force of the streamlined head, including the regions 1 and 2, make up 64% of the total force of the head car, and the regions 2, 4 and 6 above the nose accounts for 71%; however, the bogie regions 1 and 5 just constitutes about 24%. The side force coefficient of

Region 2 which is the curved surface part of the streamlined head, is highest. According to the results of the previous sections, it can be discovered that strong positive pressure by the impact of the air on the windward side and strong negative pressure by the flow separation on the windward side of the train contribute to the maximum aerodynamic side force of Region 2. For the middle car, the force of region 2 is also the largest, but its windward area is 3.7 times as big as that of region 1. The forces of these lower parts (region 1, 3 and 5) of the middle car take up 50% of the total. The force of the whole tail car is less than that of region 1 of the head car, which shows that much more attention should be paid on the aerodynamic performance of the head car and the middle car to improve the crosswind stability of the train. The force of region 2 of the tail car is negative, which is in accordance with the analysis of the train surface pressure distribution in Section 5.3. Due to this effect, it can reduce the side wind effect on the train.

For the lift force, these upper parts of the train are

positive, while these lower parts of the train are negative, which indicates the pressure is normal to the train surface and points outside in the z axis direction. The forces of the upper parts are a little larger in absolute value, which shows the strong negative pressure characteristics at the top of the train (see Section 5.3). The lift forces of each car are large, but that of the head car is the largest, and the tail car's is the least.

As for the overturning moment, it is the result of the joint action of the side force and lift force. As the moment point is the contact point between the wheels and track in the leeward side, the overall value will be smaller for the lower parts of the train, but it will not affect the analysis of the whole train. The overturning moment of the head car accounts for 53% of the total train (3 cars-grouping mode), the middle car accounts for 30%, while the car only accounts for 17%. The overturning moment of the head of the tail car is positive, indicating overturning to the opposite side of the crosswind.

6. CONCLUSION

Using the Detached Eddy Simulation technique, a numerical simulation of the high-speed train subjected to a crosswind at the 20° yaw angle has been conducted. The DES with SST $k-\omega$ turbulence model has been used to analyze the flow structures and aerodynamic loads.

The numerical results are compared with the wind tunnel experimental data from the paper written by Zhang *et al.* (2013). The DES method presents an improvement compared with the RANS simulation where a massive separation in the wake is predicted. According to the analysis of vortex structures, the evolution trends of multi-scale coherent vortex structures in the leeward side were revealed. Lots of vortex structures with different intensities, spatial geometrical scales, accompanied by a time change, appear in the leeward side of the train, in the wake of the rear car and below the bottom of the train. The streamlined head, inter-carriage gaps and bogies are all the sources of shedding vortices. These time histories of pressure coefficients at monitoring points clearly fluctuate around some certain mean values, separately. The pressure fluctuations of points on the streamlined head of the tail cars are a little larger. The oscillation characteristics of the flow field around the train directly affect the pressure change on the train surfaces, thereby affecting the aerodynamic loads of the train. To improve the crosswind stability of the high-speed train, much more attention should be paid on the aerodynamic shape design of the streamlined head and cross section. Overall, the DES method used in the paper is a good solution to simulation the flow around the high-speed train under crosswinds, which will save lots of computer resources in exploring the instantaneous characteristics of the train.

ACKNOWLEDGEMENTS

The authors acknowledge the computing resources

provided by the High-speed Train Research Center of Central South University, China.

This work was supported by the Scholarship Award for Excellent Innovative Doctoral Student granted by Central South University of China, the Project of Innovation-driven Plan in Central South University (Grant No. 2015CX003) and the National Science Foundation of China (Grant Nos. U1534210, U1334205 and 51205418).

REFERENCES

- Baker, C. J., J. Jones, F. Lopez-Calleja and J. Munday (2004). Measurements of the cross wind forces on trains. *Journal of Wind Engineering and Industrial Aerodynamics* 92, 547–563.
- Central South University (2011). Research report for train aerodynamic performance tests. Changsha: Central South University. . □
- Cheli, F., R. Corradi, D. Rocchi, G. Tomasini and E. Maestrini (2010b). Wind tunnel tests on train scale models to investigate the effect of infrastructure scenario. *Journal of Wind Engineering and Industrial Aerodynamics* 98, 353–362.
- Cheli, F., F. Ripamonti, D. Rocchi and G. Tomasini (2010a). Aerodynamic behaviour investigation of the new EMUV250 train to cross wind. *Journal of Wind Engineering and Industrial Aerodynamics* 98(4/5), 189–201.
- Copley, J. M. (1987). The three-dimensional flow around railway trains. *Journal of Wind Engineering and Industrial Aerodynamics* 26, 21-52.
- Diedrichs, B., M. Sima, A. Orellano and H. Tengstrand (2007). Crosswind stability of a high-speed train on a high embankment. *Proceedings of the Institution of Mechanical Engineers, Part F: Journal of Rail and Rapid Transit* 221(2), 205–225.
- Favre, T. and G. Efraimsson (2011). An assessment of detached-eddy simulations of unsteady crosswind aerodynamics of road vehicles. *Flow, Turbulence and Combustion* 87(1), 132–163.
- Flynn, D., H. Hemida, D. Soper and C. Baker (2014). Detached-eddy simulation of the slipstream of an operational freight train. *Journal of Wind Engineering and Industrial Aerodynamics* 132, 1-12.
- Fujii, T., T. Maeda, H. Ishida, T. Imai, K. Tanemoto and M. Suzuki (1999). Wind-Induced Accidents of Train/Vehicles and Their Measures in Japan. *Quarterly Report of Railway Technical Research Institute* 40(1), 50-55.
- Guilmineau, E., G. B. Deng and J. Wackers (2011). Numerical simulation with a DES approach for automotive flows. *Journal of Fluids and Structures* 27, 807-816.
- Hemida, H. and S. Krajnovic (2010). LES study of

- the influence of the nose shape and yaw angles on flow structures around trains. *Journal of Wind Engineering and Industrial Aerodynamics* 98(1), 34–46.
- Huang, S., H. Hemida and M. Z. Yang (2016). Numerical calculation of the slipstream generated by a CRH2 high-speed train. *Proceedings of the Institution of Mechanical Engineers, Part F: Journal of Rail and Rapid Transit* 230(1), 103-116.
- Hunt, J. C. R., A. A. WRAY and P. MOIN (1988). Eddies, stream, and convergence zones in turbulent flows. *Center for Turbulence Research Report CTR-S88*, 193-208.
- Khier, W., M. Breuer and F. Durst (2000). Flow structure around trains under side wind conditions: a numerical study. *Computers and Fluids* 29, 179-195.
- Li, Y. (2011). Experimental analysis of train aerodynamic performance in the wind field of Xinjiang. *Chinese Railways* (12), 1–3.
- Liu, T. H. and J. Zhang (2013). Effect of landform on the aerodynamic performance of high-speed train in cutting under cross wind. *Journal of Central South University* 20(3), 830-836.
- Ma, J., J. Zhang and Z. G. Yang (2008). Study on the unsteady aerodynamic characteristics of a high-speed train under cross wind. *Journal of the China Railway Society* 30(6), 109-114.
- Mao, J., Y. H. Xi and G. W. Yang (2011). Research on influence of characteristics of cross wind field on aerodynamic performance of high-speed train. *Journal of the China Railway Society* 33(4), 22-30.
- Matschke, G., T. Tielkes, P. Deeg and B. Schulte-Werning (2000). Effects of Strong Cross Winds on High-Speed Trains – a Risk Assessment Approach. *Proceedings of the 5th International Conference on Probabilistic Safety Assessment and Management*, Osaka, 27,1.
- Miao, X. J. and G. J. Gao (2012). Aerodynamic performance of train under cross-wind based on DES. *Journal of Central South University (Science and Technology)* 43(7), 2855-2860.
- Nakade, K. (2014). Numerical Simulation of Flow Around Railway Vehicle in Turbulent Boundary Layer over Flat Terrain. *Quarterly Report of Railway Technical Research Institute* 55(4), 249-253.
- Orellano, A. and M. Schober (2006). Aerodynamic Performance of a Typical High-Speed Train. *Proceedings of the 4th WSEAS International Conference on Fluid Mechanics and Aerodynamics*, Elounda, Greece, August 21-23, 18-25.
- Osth, J. and S. Krajnovic (2014). A study of the aerodynamics of a generic container freight wagon using Large-Eddy Simulation. *Journal of Fluids and Structures* 44, 31-51.
- Spalart, P. R., W. H. Jou, M. Strelets, S. R. Allmaras (1997). Comments on the feasibility of LES for wings, and on a hybrid RANS/LES approach. *Proceedings of first AFOSR international conference on DNS/LES*, Ruston, Louisiana. Greyden Press 4–8.
- Sterling, M., C. J. Baker, S. C. Jordan and T. Johnson (2008). A study of the slipstreams of high-speed passenger trains and freight trains. *Proceedings of the Institution of Mechanical Engineers, Part F: Journal of Rail and Rapid Transit* 222, 177–193.
- Tanemoto, K., M. Suzuki and H. Fuji (2006). Wind tunnel experiments on aerodynamic characteristics of vehicle crosswind. *Railway Research Review* 63(8), 28-31.
- Tian, H. Q. (2007). Train aerodynamics. Beijing: China Railway Publishing House.
- Wang, Y., Y. Xin, Z. h. Gu, S. h. Wang, Y. Deng and X. Yang (2014). Numerical and Experimental Investigations on the Aerodynamic Characteristic of Three Typical Passenger Vehicles. *Journal of Applied Fluid Mechanics* 7(4), 659-671.
- Yang, Z. G., J. Ma, Y. Chen and J. Zhang (2008). The unsteady aerodynamic characteristics of a high-speed train in different operating conditions under cross wind. *Journal of the China Railway Society* 32(2), 18-23.
- Yao, S. B., D. L. Guo, Z. X. Sun, G. W. Yang and D. W. Chen (2014). Optimization design for aerodynamic elements of high speed trains. *Computers and Fluids* 95, 56-73.
- Zhang, J., G. J. Gao and L. J. Li (2013). Height optimization of windbreak wall with holes on bridge of high-speed railway. *Journal of Traffic and Transportation Engineering* 13(6), 28-35.
- Zhang, J., G. J. Gao, T. H. Liu and Z. W. Li (2015). Crosswind stability of high-speed trains in special cuts. *Journal of Central South University* 22(7), 2849-2856.
- Zhang, J., J. J. Li, H. Q. Tian, G. J. Gao and J. Sheridan (2016). Impact of ground and wheel boundary conditions on numerical simulation of the high-speed train aerodynamic performance. *Journal of Fluids and Structures*. 61, 249-261.
- Zhang, J., X. F. Liang, T. H. Liu and L. F. Lu (2011). Optimization Research on aerodynamic shape of passenger car body with strong crosswind. *Journal of Central South University (Science and Technology)* 42(11), 3578–3584.

□